5-13-2022

Analysis of comet rotation through modeling of features in the coma

Ien Harris
iaharris423@gmail.com

Analysis of comet rotation through modeling of features in the coma

By

Ien Harris

Approved by:

Donna M. Pierce (Major Professor)
Angelle Tanner
Torsten Clay
Henk F. Arnoldus (Graduate Coordinator)
Rick Travis (Dean, College of Arts & Sciences)

A Thesis
Submitted to the Faculty of
Mississippi State University
in Partial Fulfillment of the Requirements
for the Degree of Master of Science
in Physics
in the Department of Physics and Astronomy

Mississippi State, Mississippi

May 2022

Name: Ien Harris

Date of Degree: May 13, 2022

Institution: Mississippi State University

Major Field: Physics

Major Professor: Donna M. Pierce

Title of Study: Analysis of comet rotation through modeling of features in the coma

Pages of Study: 54

Candidate for Degree of Master of Science

An integral field unit fiber array spectrograph was used to observe the emission spectra of radical species (C_2, C_3, CH, CN, and NH_2) in multiple comets. The resultant azimuthal and radial division maps produced from the reduced data provide a unique method of analyzing features with these radicals in the comae, as well as how they behave over time. A Monte Carlo model was developed in order to simulate the behavior of particles from the outer nucleus and coma of each comet depending on various parameters including rotational period, outflow velocity, and active area location. The results from the model were used to constrain the physical parameters of three comets: 10P/Tempel 2, C/2009 P1 (Garradd), and 168P/Hergenrother.

DEDICATION

To Cat, Pot Roast, Lizzie, and Daisy. Oh and thank you to Katie too I guess.

ACKNOWLEDGEMENTS

We acknowledge use of the JPL HORIZONS system for all comet ephemerides.

This material is based upon work supported by the National Aeronautics and Space Administration under Grant No. NNX14AH18G.

This paper includes data taken at the McDonald Observatory of the University of Texas at Austin. The observations were supported under NASA Grants No. NNX08AO52G and NNX17AI86G.

TABLE OF CONTENTS

LIST OF TABLES

LIST OF FIGURES

CHAPTER I

INTRODUCTION

Scientists across multiple fields, not just physics and astronomy, have an interest in comets and their connection to the formation of the solar system. Many questions concerning the chemical and biological evolution of life on Earth involve the early conditions of the planet. Accretion of material in the outer distances of the solar system led to the formation of comets. Initially postulated as "dirty snowballs" [40], recent observations of the composition of comets led astronomers to view them more as "icy dirtballs", consisting mainly of ice, rock, and organic compounds that coalesced together into low density structures during the early age of the solar system, over 4.5 billion years ago [3]. This composition appears to hold true even for observed insterstellar comets, such as 2I/Borisov [8], which was observed passing through our solar system in 2019. Comets are usually grouped by their orbital characteristics, with the longer-period comets originating from distant small-body populations such as the Kuiper Belt, the scattered disk, and the Oort Cloud. The existence of these populations support a model of the evolution of the solar system known as the Nice model, where the gas giants were in more cicular, closely spaced orbits at the edge of the inner disk. Small icy bodies were scattered by the gas giants inwards, which caused Saturn, Uranus, and Neptune to migrate outwards due to conservation of angular momentum [38]. Further interactions with Jupiter caused the icy bodies to enter highly elliptical orbits, while Jupiter migrated slighty inwards

towards its current postion. An alternative model known as the grand tack hypothesis proposes that Jupiter instead initially migrated inwards from a distance of 30 AU and then outwards after capturing Saturn in a mean-motion resonance [26]. This hypothesis has developed more recent support from studies of comets C/2014 S3 (PANSTARRS) and 67P/Churyamov-Gerasimenko, where the low detection of collisional elements in these outer bodies corresponds with the early migration of Jupiter and Saturn posited in the grand tack [37].

Comets tend to be less dynamically active and exhibit less change in volatile composition compared to other major bodies in the solar system. Thus, they provide insight into the physical and chemical properties of the early conditions of the solar system. *In situ* measurements of comets, such as the *Stardust* mission, have detected organic molecules, including the amino acid glycine [9]. Such evidence supports the hypothesis that comets were key to delivering the precursors to life to early Earth. However, recent studies into comets, including the *Rosetta* mission, have measured the Deuterium-to-Hydrogen (D/H) ratio, which was determined to be at least three times greater than the ratio for the Vienna Standard Mean Ocean Water (VSMOW) on Earth, $(1.5576 \pm 0.0001) \times 10^{-4}$ [27]. This suggests the opposite to the long-held idea that comets were also the means through which water came to our planet. Cometary science is still rapidly changing and can still provide much in the way of constraints of the formation of Earth and the solar system.

The majority of comets fall within two categories: short-period and long-period comets, based on whether their orbital revolution periods are less than, or greater than, 200 years. Most short period comets, known as Jupiter-family comets (JFCs), are theorized to have originated from beyond Neptune, in the scattered disk of the Kuiper Belt region. They tend to orbit in the same ecliptic plane as the planets and have periods of less than 200 years. The exception to these are the

Halley-family comets. While they also have a short orbital period, they are highly inclined to the ecliptic, suggesting a different region of origin: the distant Oort Cloud. Proposed by Jan Oort in 1950, the Oort Cloud is a theoretical, spherical region of space dominated by icy planetesimals that were theorized to have formed during the same time period as the planets [32] [10]. Long-period comets by contrast are highly eccentric, leading to orbital periods that range from hundreds to thousands of years. These long-period comets are also thought to have originated from the Oort Cloud. As many have hyperbolic trajectories, long-period comets will only have a single solar apparition before they escape the solar system.

Due to their possible connection to the formation of the solar system, comets are the subject of numerous chemical surveys [15]. Narrow-band photometry [1] and spectroscopic surveys [7] have shown that the majority of comets are similar in chemical composition, with the exception that a significant fraction of JFCs are depleted in carbon-chain molecules. Observations of the dust-to-gas ratio and the abundances of carbon-based radical species (CN, C_3, C_2, etc.) show little correlation based on composition or dynamical family. The subtle variances exhibited in the comets based on their classes suggest differences in dynamical evolution rather than different conditions of formation [7].

Due to the nature of comets, many properties have to be inferred from the types of radiation we can detect remotely, as *in situ* observations are a rare opportunity. One such property is the rotational period of the comet, which has most commonly been determined from the measured lightcurve. If a celestial target such as a comet is observed over a long enough period, it is possible to graph the flux or intensity of the measured light over time. If periodicity is seen in the lightcurve, then it is possible to determine a spin period of the nucleus. Further constraints could be made if

multiple lightcurves are made over a range of heliocentric distances, as was made with 1P/Halley [14]. Active areas are determined from spherical nucleus approximations, even though they tend to be elliptical in nature. Constraints are made based on the size and flux of emission sources, and are determined as fractions of the surface area of the nucleus [20].

1.1 Target comets

The comets examined in this research were C/2009 P1 (Garradd), Comet 168P/Hergenrother, and Comet 10P/Tempel 2. Garradd was an active, dynamically young, long-period comet at the time of observation, likely making its first trip through the solar system. The comet is in a highly eccentric orbit of e = 1.001, and has an inclination of 106.18 degrees. Comet Hergenrother is a Jupiter-family comet with an orbital period of about 6.90 years. It has an orbital eccentricity e = 0.610, and an inclination of 21.93 degrees. Tempel 2 is also a JFC, with e = 0.5363, an inclination of 12.02 degrees, and an orbital period of about 5.5 years.

Comet Garradd was very active during its pre-perihelion transit, with one of the highest dust-to-gas ratios and water production rates observed in a comet [5]. The CO_2/H_2O and CO/H_2O ratios were measured from September-October 2011, and in January-March 2012, and were found to be less abundant post-perihelion [5]. Since the ices in comets are primarily composed of these volatiles, we can determine how the activity is driven during the comet's passage. An asymmetry between the two ratios from pre- to post-perihelion also suggests either a large-scale chemical heterogeneity in the nucleus [30], or that the rotational state led to an effect where one hemisphere was exposed to more activity from solar exposure than the other [13]. It also had a high active surface area to nucleus area ratio.

Comet Hergenrother was a recently discovered comet, of which few publications exist. It underwent an outburst in 2012, which may have resulted in a fragmentation event a few weeks afterward and has been reported as overdue for its 2019 apparition after it was not detected near its expected perihelion passage. [41]. Pierce and Cochran [33] performed spectroscopic analysis of Hergenrother and found it to be the most depleted comet reported in C_2, C_3, and NH_2. Observations of such events can provide unique insight into the chemical and physical properties of comets during a period of high activity. Fragments of Comet 73P/Schwassmann-Wachmann 3 were observed to have similar chemical properties but physical heterogeneities [16]. The fragmentation event itself can also affect the dust production, such as with C/1994 S4 LINEAR [2], or the orbital parameters, as with the Kreutz sungrazers, a family of comets believed to have originated from a common progenitor comet that fragmented into two parts during a past perihelion approach within 3.45 solar radii [19]. These super-fragments were then believed to have undergone their own fragmentation events upon subsequent perihelion passages [36].

In contrast, 10P/Tempel 2 has been extensively studied since its discovery in 1873. Its short orbital period, allowing for multiple observations over dozens of apparitions, as well as it once being a possible target for a flyby mission, has made it the object of numerous ground-based studies. Its next close approach to Earth is due to occur in August 2026 with a nominal geocentric distance of 0.41 AU. It has been observed to have low outgassing activity and brightness pre-perihelion, and has a typical dust-to-gas ratio of other comets with a similar perihelion distance [23].

CHAPTER II

OBSERVATIONS

Observations of comets primarily focus on two components: the nucleus and the coma. The nucleus corresponds to the solid part of the comet. Nuclei are typically comprised of dust and ice, and tend to have a size range on the order of a few to tens of kilometers. As the nucleus is exposed to heat from the Sun, the ices trapped on or below the surface can sublimate. The resultant atmosphere of gas surrounding the nucleus is known as the coma. As the comet approaches the Sun, the visible coma can increase in size to an order of tens of thousands of kilometers in diameter, as ice grains can continue to sublimate as they're dragged outwards by the gas. Due to the low albedo and smaller size of the nucleus compared to the coma, direct observations of the nucleus are usually restricted to in situ measurements. For comets Garradd and Hergenrother, the measurements for this study were taken of their respective comae from ground-based telescopic observations. The observations for Comet Garradd were obtained pre-perihelion, while the Hergenrother and Tempel 2 observations were obtained post-perihelion. Specific observation and calibration parameters for Garradd, Hergenrother, and Tempel 2 are shown in Table 2.1 and Table 2.2 on page 8.

The coma observations were obtained with the George and Cynthia Mitchell Spectrograph. This integral-field unit (IFU) spectrograph is a low- to moderate- resolution fiber optic spectrograph consisting of 246 optical fibers. The optical fibers each have a diameter of 4.1 arcsec and are

arranged in a 1.7 x 1.7 arcmin array, alternating from 14 to 15 bundled fibers per row [17]. A diffraction grating covered the passband from 3600-5800 Å and provides a spectral resolving power ($\lambda/\Delta\lambda$) of 850. The spectrometer was used in conjunction with the 2.7 m Harlan J. Smith Telescope located at McDonald Observatory in Fort Davis, Texas. In order to maintain the comet's position on the array, a tracking star is used with a fiducial that moves opposite to the comet's motion. Any star spectra caught crossing through the field of view are removed in analysis [33].

Observations were taken of various radical species with spectral emission bands visible in the spectrometer's passband, including C_2, C_3, CH, CN, and NH_2. Each fiber in the array was connected to a charge-coupled device (CCD) and yield independent spectra. The raw data were initially reduced through bias subtraction, flat fielding, and calibration in flux and wavelength. Since the measured spectra are a mix of the emission bands from the coma superposed on a continuum from the reflection of the solar spectrum off the dust in the coma, analogue stars were utulized. Each night the flux and color of a solar analog star is matched with the observed comet's spectrum, and the solar spectrum is subsequently removed.

Table 2.1

Comet Observation Parameters

Comet	Obs. Date (UT)	r_H[1] (AU)	Δ[2] (AU)	Phase Angle[3] (Degrees)	Pre/Post Perihelion
10P/Tempel 2	2010 Jul 15	1.43	0.72	42.2°	Post
	2010 Sep 13	1.60	0.67	21.8°	Post
C/2009 P1 (Garradd)	2011 Aug 20	2.28	1.40	16.1°	Pre
	2011 Aug 21	2.27	1.39	16.4°	Pre
	2011 Aug 22	2.26	1.39	16.9°	Pre
168P/Hergenrother	2012 Oct 6	1.42	0.44	14.8°	Post
	2012 Oct 8	1.42	0.44	16.1°	Post
	2012 Oct 9	1.42	0.44	16.7°	Post
	2012 Dec 19	1.66	0.99	32.7°	Post
	2012 Dec 20	1.66	0.99	32.7°	Post
	2012 Dec 21	1.67	1.00	32.7°	Post

Table 2.2

Comet Calibration Targets

Comet	Obs. Date (UT)	Flux Standard	Solar Analogue
10P/Tempel 2	2010 Jul 15	Feige 98	None
	2010 Sep 13	BD+25 3941	HD 191854
C/2009 P1 (Garradd)	2011 Aug 20	BD+25 3941	39 Tau
	2011 Aug 21	Feige 15	HD 6204
	2011 Aug 22	BD+28 4211	HIP 109931
168P/Hergenrother	2012 Oct 6	Feige 15	HD 19518
	2012 Oct 8	BD+28 4211	HIP 109931
	2012 Oct 9	BD+28 4211	16 Cyg B
	2012 Dec 19	Feige 15	Hyades 64
	2012 Dec 20	Feige 34, Feige 56	35 Leo
	2012 Dec 21	Feige 15, Feige 25	Hyades 64, HD19518

The reduced data were separated into columns representing the fiber number, the base-10 logarithm of the projected distance from the comet nucleus ($log(\rho)$), the logarithm of the column density of the respective radical ($log(N)$), and the x and y coordinates of the coma measurement from the comet nucleus. For the Garradd and Hergenrother data, x corresponded to the hour angle offset in kilometers, and y corresponded to the declination position in kilometers. The radial distance from the comet nucleus, ρ, was determined by the distance formula

$$\rho = \sqrt{x^2 + y^2} \tag{2.1}$$

The optocenter fiber was determined from each observation from the fiber corresponding to the lowest value of ρ. This single fiber is designated as the position of the comet nucleus.

Raw contour plots were generated for each observation, with the variables corresponding to the x and y values for each observation, and the contour levels corresponding to the $log(N)$ values. The data were then analyzed based on their arrangement about the optocenter. In order to model enhanced coma features as a function of projected distance from the nucleus, azimuthal rings were determined based on the fibers being arranged in concentric, hexagonal rings about the optocenter. For each pixel in the ring, the projected distance was measured from the optocenter by

$$|\rho - \rho_0| = \sqrt{(x - x_0)^2 + (y - y_0)^2} \tag{2.2}$$

where x_0 and y_0 represent the horizontal and vertical position of the optocenter, and x and y represent the horizontal and vertical position of the respective pixel. For each pixel in each azimuthal ring, the values for $|\rho - \rho_0|$ were averaged, yielding an averaged radius value (ρ_{avg}). The column densities for each fiber in the ring were also averaged, yielding an azimuthally averaged column

density value N_{avg}. In order to describe the relationship of the column density of each radical with respect to the projected distance from the nucleus, a relationship N_{model} was determined,

$$N_{model} = C|\rho - \rho_0|^k, \tag{2.3}$$

where C and k are constants determined from a weighted least-squares fit. The fit parameters were determined from the linear relation

$$\log(N_{model}) = k \log(|\rho - \rho_0|) + \log(C) \tag{2.4}$$

To further examine the heterogeneities of the radicals, azimuthal division coma enhancement plots were generated, with the contour levels corresponding to the column density N of each fiber divided by the respective N_{avg} of the azimuthal ring. Radial division coma enhancement plots were generated in a similar manner, with the contour levels corresponding to the ratio of N over N_{model} for each fiber in the array.

These azimuthal and radial coma enhancements can be used to look for coma features such as jets or arcs. In addition to comparing coma features for each radical species across different comets, they can also be used to observe how these features change over time. By focusing on how the features change in position over several observations, we can attempt to link coma features with changes in the physical nucleus, and recurring coma morphological features can be used to constrain possible rotational states of the comets. The most common way to constrain comet rotation periods is through analyzing a measured lightcurve to look for periodic, repeating behavior [31]. A technique similar to ours used by Esterle [11] with Comet Halley involves dynamically modeling simulated dust jets about the long axis mode of the comet nucleus over time, and comparing them with jets seen in ground-based observations. Comparing spectroscopic

features allows for an additional method of analyzing rotation by use of a Monte Carlo model [22]. Comparisons between the raw, azimuthal division, and radial division contour plots are shown in Figure 2.1 on the next page.

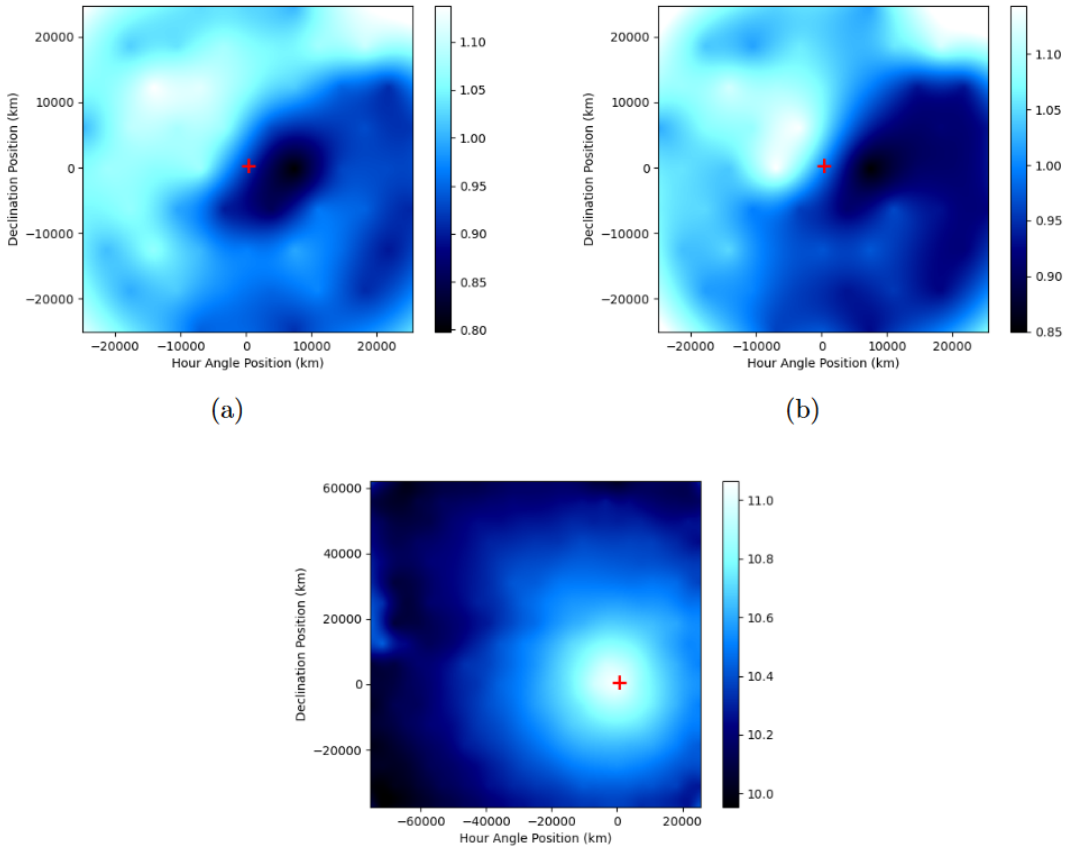

Figure 2.1

Sample IFU contour plots

Representations of the radially divided (a) and azimuthally divided (b) contour plots (top) with their respective raw contour plot (bottom). Plots were of C_3 measurement taken from Comet Garradd on 2011 August 22. The raw plot is slightly offset in terms of the origin, as it is aligned with the optocenter (denoted by the red crosshair) of the fiber array.

CHAPTER III

METHODS

There are no simple methods for analyzing the mechanical behavior of the comet, such as its rotational motion, from the radical features expressed in the outer coma. We can, however, place constraints on several parameters by simulation. A Monte Carlo model used by Schleicher and Woodney [35] outlines a method by which we can use the properties of the detected dust particles of our radical species and their motion over time to simulate the behavior of the features found in our coma enhancement plots. Several parameters of the model can be adjusted manually, and they are usually randomly generated within known boundaries. These include the positions of the simulated active regions, the number and position of the particles within these respective active regions, their outflow direction and velocity, and the rotational axis of the comet, assuming no precession or nutation. Each run of the model will output several images over a predetermined period of time that corresponds with the timespan of the comet observations.

The model is used to simulate a variety of cases, with the parameters randomly varied between each simulation [35]. The visual output of the model is then cross-referenced with the comet enhancement plots by eye in order to determine a reasonable range of values for the parameters. They are then adjusted slightly to yield a better overall fit of the simulated particles with the

features shown in the enhancement plots. With these determined physical parameters, it is possible to constrain a rotational period for the comet.

3.1 The model

The outline for the Monte Carlo model involves generating a simplified, spherically symmetric model of the nucleus in 3-dimensional space. The model must be initialized with several parameters including pole orientation, latitudes and longitudes of jet features, outflow velocity of radical particles, and a set rotational period. A fixed number of particles are generated within the 3D space, on the order of 10^4. To determine if features in the outer coma are related to physical active regions on the surface of the comet's nucleus, we assume that they are the same quantity. These particles represent dust grains from active regions of a spherically-symmetric nucleus. The size of the comet nucleus is based on available literature for the target comet being studied. Otherwise, if no published values exist, we work within a likely range of values for those comets. The fraction of the nucleus that is considered active is determined by a pseudo-random number generator operating within a range of 10 - 60%. The active fraction is constrained to one or more regions with randomly generated sizes and positions on the nucleus, depending on how many possible active regions can be determined from the enhancement plots. Particles that are located within the boundaries of the active regions are sorted into a separate list from the 'inactive' particles, and are made visually distinct in the output plots via differing colors. A location for the solar vector is set based on the comet's orbital ephemeris at the time of observation. The chance that a particle is released from the nucleus and emitted into the coma is determined by a probability function of the cosine of the angle between the respective particle's position and the solar vector. If the particle is released from

the nucleus, its outflow position and velocity are tracked as it is emitted into the coma. The outflow dispersion angles for the particles are defined by a random Gaussian distribution.

At the same time, the movement of the active regions due to the rotation of the comet is simulated based on a predetermined rotational axis. For the sake of this model, a simple rotational state is assumed, with no effects due to precession or nutation. Since the detected features from our observations may not move at the same rate as the comet's physical nucleus, we cannot simply assume that our rotation parameter is the same value as the actual rotational period.

Additional perturbations on the released particles exist in the form of solar radiation pressure. For real comet dust grains, the pressure applied by radiation from the Sun has a non-negligible effect. The pressure (in N/m^2) on each particle can be determined by

$$P_{rad} = C_{rad} \frac{G_{SC}}{c} \frac{\vec{r_d}}{|\vec{r_d}|^3} \tag{3.1}$$

where G_{SC} is the solar constant: 1361 W/m^2, and $\vec{r_d}$ is the displacement vector between each particle and the Sun. C_{rad} is a constant where 2 corresponds to a perfectly reflecting surface, and 1 corresponds to perfect absorption. In reality, materials are neither totally reflecting nor absorbing, so C_{rad} is randomly generated close to a value of 1, as dust grains tend to have low albedos. The pressure is then multiplied by the cross-sectional area and divided by the mass for each particle to determine the subsequent applied acceleration. For the scales of these particles, we assume a mass on the range of 10^{-6} kg, and radii within a range of 0.1 μm to 1 mm [34]. A flowchart showing the step-by-step processes for the model is shown in Figure 3.1 on the following page.

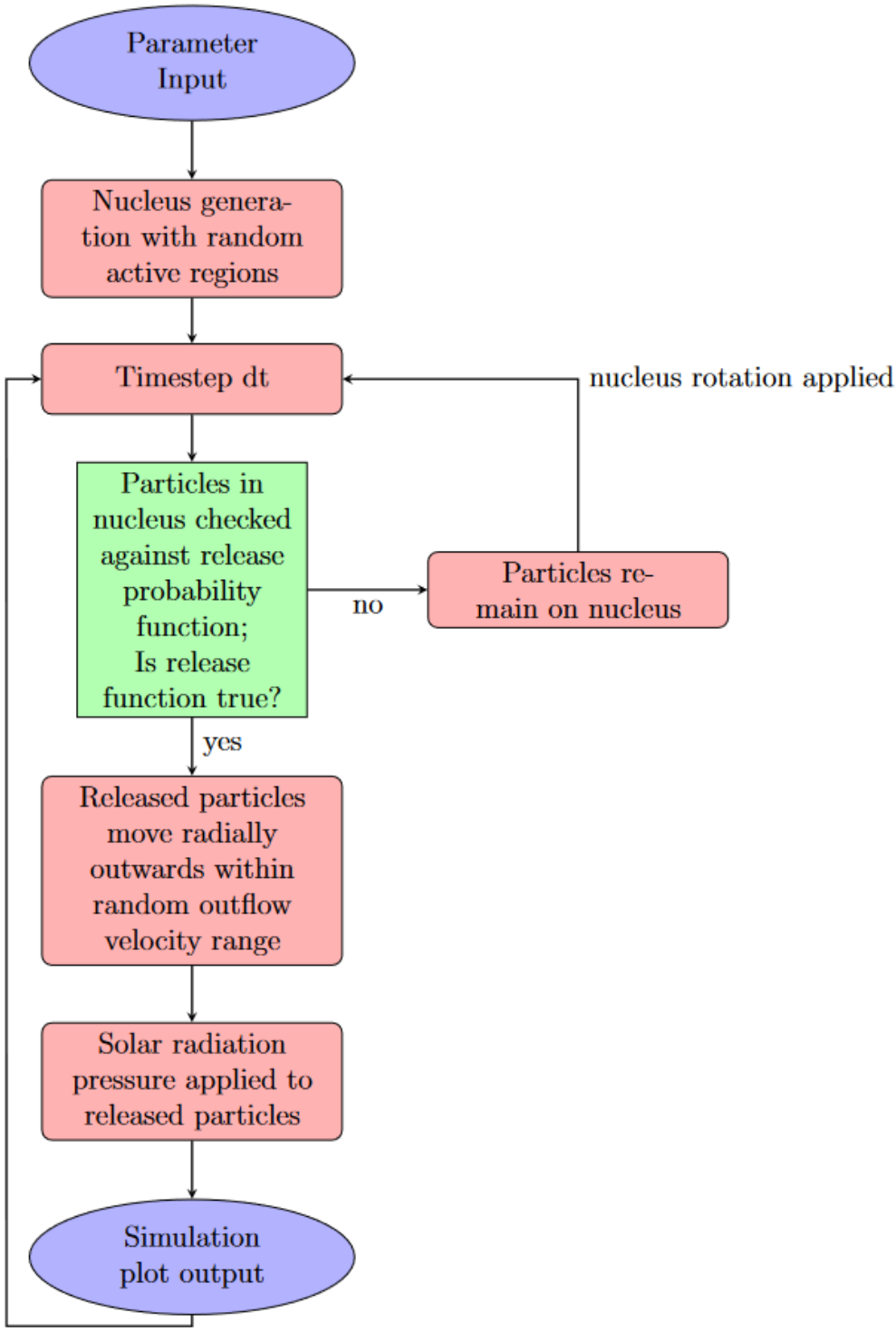

Figure 3.1

Flowchart for model processes

3.2 Determining a limit for outflow velocity

One of the parameters that must be accounted for in the Monte Carlo model is the mean outflow velocity of the radicals as they move outwards from the nucleus. Since there is no simple, common factor amongst comets with regards to this behavior, we must try to determine it by analyzing the positions of the emitted particles over time.

We use a similar method as [35] to constrain a velocity from our radial profile data. They divided their enhanced division plots, obtained through narrowband photometry, into 10° wedges, yielding 36 wedges in total. For each of these wedges that coincided with specific morphological features in the coma, they examined the brightest points and tracked their relative positions over the timespan of their observations. Due to the discrete, separated nature of our fiber array spectrograph, as opposed to their CCD detector, we must use twelve 30° wedges to ensure sufficient data are contained in each wedge. We tracked the radial position of the point corresponding to the highest measured N_{rad} (where N_{rad} is the ratio between the column density N and the modeled column density related to the projected radius from the optocenter, N_{model}) for constant features over the timespan of all of our observations for each night. The radial positions for the carbon-bearing radicals, such as C_2 and CN, were grouped together to increase the amount of available data.

These positions were plotted with respect to the difference in time from the first observation for each usable 30° wedge. A line of best fit was found for each using linear regression, as shown in Figure 3.2 on page 19. By comparing the regression slope parameters of each wedge for each night, we can determine an upper limit on the mean outflow velocity of the particles from the nucleus. This, in turn, can be used as a parameter to better model the outflow behavior of the particles in our

Monte Carlo simulation. This process is repeated for each identified active region in the comet's coma.

As the dust particles get farther from the nucleus, forces such as solar radiation pressure and gravity start to dominate [28]. These additional parameters must then be accounted for and calculated based on each simulated particle's relative position to the comet nucleus and the solar angle.

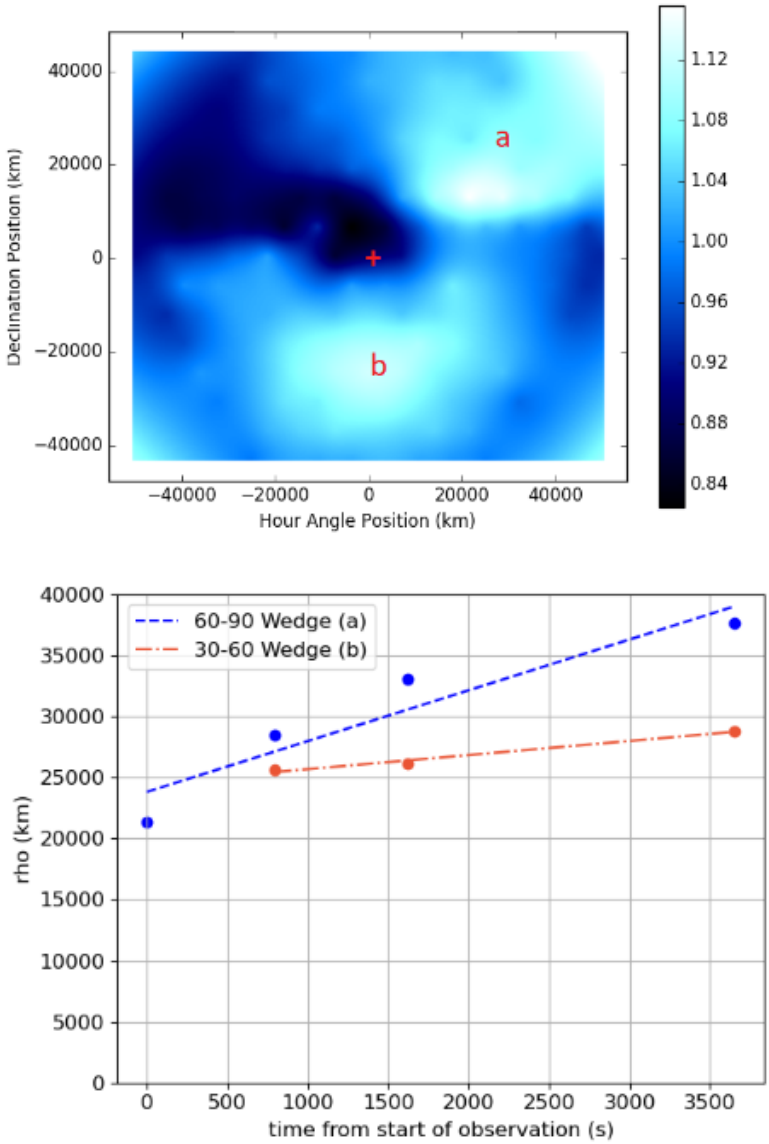

Figure 3.2

Outflow feature angular positions

Angular positions of detected features over the timespan of the observations of Comet Garradd. The above figure depicts an example CN radial division map, and the bottom figure shows the position vs time relation for CN over all observations. The color bar scale on the upper map represents the column density of CN. The blue line of the bottom figure represents feature (a), while the orange line represents feature (b)

3.3 Comparing spatial concentrations

While a qualitative method of visually comparing the model results with enhancement plots was established, a more quantitative approach was desired as well. A method outlined by Vaughan [39] for analysis of comet data from the same IFU spectrometer was utilized, where the enhancement plots were divided into a circle with symmetrical 60° wedges, centered on the optocenter fiber. The fibers that were located in these position angle wedges were used to calculate the concentration ratio Ω,

$$\Omega = \left(\frac{AziDiv}{\sigma^2_{AziDiv}} + \frac{RadDiv}{\sigma^2_{RadDiv}} \right) \left(\frac{1}{\sigma^2_{AziDiv}} + \frac{1}{\sigma^2_{RadDiv}} \right)^{-1} \tag{3.2}$$

where *AziDiv* and *RadDiv* correspond to the weighted averages of the azimuthal division values and the radial division values, respectively, for each fiber. A larger number of fibers within each wedge allows for more accurate values of Ω, which is why 60° wedges are used, as opposed to the 30° wedges used in the outflow velocity determinations. If a fiber resides exactly on a line dividing the wedges, the concentration values are determined from the weighted average of two symmetric fibers along either boundary of the wedge.

$$\Omega = \left(\frac{AziDiv_1}{\sigma^2_{AziDiv,1}} \frac{AziDiv_2}{\sigma^2_{AziDiv,2}} + \frac{RadDiv_1}{\sigma^2_{RadDiv,1}} \frac{RadDiv_2}{\sigma^2_{RadDiv,2}} \right) \left(\sum \frac{1}{\sigma^2} \right)^{-1} \tag{3.3}$$

where the summation term is

$$\sum \frac{1}{\sigma^2} = \frac{1}{\sigma^2_{AziDiv,1}} + \frac{1}{\sigma^2_{AziDiv,2}} + \frac{1}{\sigma^2_{RadDiv,1}} \frac{1}{\sigma^2_{RadDiv,2}}$$

The average Ω values are then calculated for each wedge for each moment of observation. The Ω_{avg} values for each comet and observation are shown in Appendix A. This method is known as Welch's Analysis of Variance (ANOVA).

Since the model does not simulate discrete fibers, the concentration is simply determined by dividing the final output into 60° wedges and calculating the ratio of the number of particles in each wedge with the overall total particles produced for the simulated comet nucleus. With concentration values organized in this way, we now have an additional method of comparing the model results with our observed enhancement plots after they have been initially constrained by eye.

CHAPTER IV

RESULTS

The rotation of the comet is accounted for by setting a principal axis of rotation and including a parameter for a change in angular position for set time-step intervals. Each time-step of the model corresponds to the observations from the IFU spectrograph. For each time-step, the particles within the active regions are checked against the release probability function. If they pass the check, they are emitted radially outwards from the nucleus. If they do not pass, the particle remains on the nucleus as it rotates in each interval. This process is repeated for every time-step, with the emitted particles continuing their outward motion based on the outflow velocity values. Non-released particles have a chance to pass the release probability check with every step.

The outputs from the three-dimensional model are manually analyzed in a two-dimensional grid to compare with the observable features as seen on the plane of the sky in the 2-D contour plots. The rotational period of our coma model was adjusted until we were able to approximate an acceptable fit to our observations obtained with the IFU. A sample output of the model is shown in Figure 4.1 on the following page.

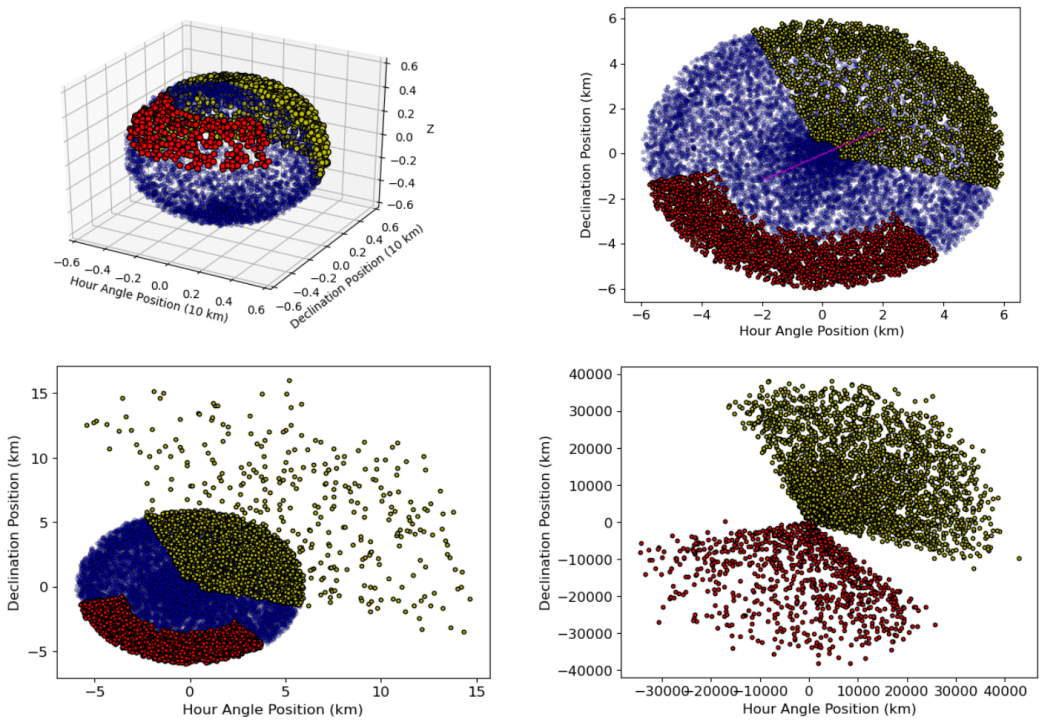

Figure 4.1

Sample nucleus of model

The top left image shows an initial setup in three dimensions, while the figure on the top right depicts the respective setup in two dimensions, with the z-axis increasing out of the page as the nucleus would be seen on the plane of the sky. The colored circles represent the modeled particles. Inactive particles are blue, and the separate active regions are shown in red and yellow. The two-dimensional plots are primarily used to compare our results with the IFU observations. The bottom figures represents subsequent timesteps.

4.1 10P/Tempel 2

Comet 10P/Tempel 2 is a Jupiter-family comet that was observed with the IFU spectrograph. Tempel 2 has been a subject of much analysis from outside sources [23], making it a useful body for comparison. The effective radius of the nucleus was determined to be 5.98 ± 0.04 km [24], which is very large for a JFC. The rotation period was determined to be 8.950 ± 0.002 hours by Knight et al. [21] at the time of its 2010/2011 perihelion approach. Furthermore, the period was also determined to have increased slightly between perihelion passages in 1988 and 1999, possibly due to systematic torque [23].

From our radial division maps for the carbon-bearing radicals of Tempel 2, we were able to determine one large primary feature in the coma, as shown in Figure 4.2 on page 27. This area of high column density was present in our observations from 2010 July 15 and September 13, suggesting they are from the same active source. The angular position of the feature changes very little between observations taken on each date, suggesting that the active region from which it originates is located near a rotational pole. A similar feature was observed from the NH_2 radial division maps, though it is smaller in size.

Our Monte Carlo model was constrained to see if similar conditions could be observed from the output. Thirty cases were produced from a parameter range, and the best fit was visually chosen from among them. The parameters used for the final Tempel 2 simulations are shown in Table 4.1 on page 26. The resulting images are shown in Figure 4.3 on page 28

Tempel 2 illustrates one of the main limitations with our model: working with a small number of observations. Tempel 2 was observed with the IFU spectrograph for only two nights, both with a small temporal range. Observation times are detailed in Table 4.2 on page 26. As comet rotational

periods tend to be at least several hours long, the available observations only offer a glimpse at the spatial behavior for comparison with the simulation results. Furthermore, coma plots from each enhancement date show only a single feature for all radical species, limiting our ability to constrain our simulated plots by our usual visual standards.

Table 4.1

Tempel 2 Model Parameters

Parameter Name	Value	Source
Radius	6 km	Lamy & Toth et al. 2009 [24]
Outflow velocity	0.6 km/s	Knight et al. 2012 [23]
Solar Vector Angle	109°	NASA Horizons
Rotation period	8 ± 0.5 hours	Custom parameter output
Active Area Fraction	34.3 ± .01 %	Random parameter output
Number of test cases	30	Result

Table 4.2

Observation times for Tempel 2

Observation Label	Start Time (UTC)	
July 15 2010		
278	08:39	300
279	08:48	600
280	09:03	900
September 13 2010		
400	09:08	600
401	09:22	900
402	09:39	900
407	11:08	900
408	11:25	600

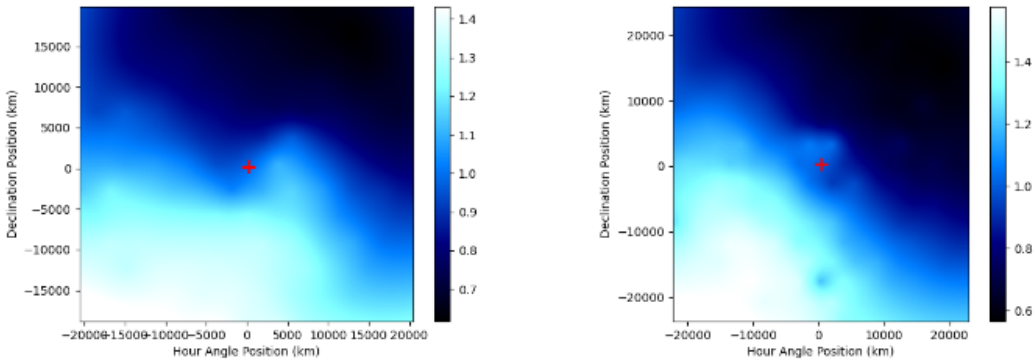

(a) 15 Jul 2010 (b) 13 Sep 2010

Figure 4.2

Radial division maps for CN in Tempel 2

The large active feature can be seen in the lower left in both the July (left) and September (right) observations, suggesting little dynamic activity in this period of the comet's orbit.

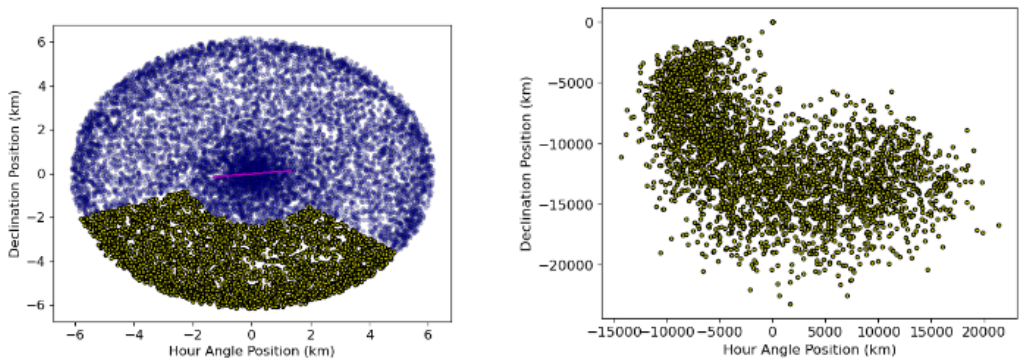

Figure 4.3

Plots for Comet Tempel 2 from the Monte Carlo model

The first image shows one of the earliest time-steps for the simulation, while the last shows the resultant plot after a simulated passage of a little over 8 hours. The purple line running through the nucleus in the left plot denotes the simulated primary rotation axis, which is partially perpendicular to the plane of the figure.

4.2 C/2009 P1 (Garradd)

Our observations of comet Garradd showed a continuous feature present in the upper right quadrant of the division maps for the carbon-bearing radicals, as seen in Figure 4.4 on page 32. This suggests a relatively simple rotational mode for the comet, with the feature possibly originating near the pole of the primary rotational axis. As such, we first tested our simulation by inputting parameters from Garradd that were observed and also supported by other sources. These are given in Table 4.3 on page 31. Due to the appearance of two features, a wider test case of about seventy runs was required for a best-match simulation. Observation times are shown in Table 4.4 on page 31, with each observation having a 600 second duration.

Figure 4.5 on page 34 shows comparisons between sample radial division plots and model simulation results that most visually resemble them. The simulated total active area fraction was generated as 49.5%, which would support our estimate that Garradd is a highly active comet. The water production rates measured by Boissier et al. [6] suggests an active area fraction of at least 50%. One notable distinction from the model output is the lower concenctration of particles in the feature in the bottom of the map for Figure 4.5b. This can be due to limitations with the model, or it could indicate a more complex rotational mode for Garradd than was initially assumed, as the feature is not present for the entire night of observations. It could also be due to the fact that the simulated nucleus is stationary, with the only motion being due to rotation. In reality, the comet is travelling through space as it orbits the Sun, so if an active jet were to rotate away from view, we wouldn't still be seeing all the residual outflow. All the carbon-bearing radicals appear to have similar morphologies over our observation period, suggesting they originate from the same source regions on the surface of the nucleus. CN is typically chosen for primary visual comparison, as

it has a better contrast in the coma compared to the other radicals due to the strength of the violet band [23].

The concentration ratio of the active particles in the simulation shown in Figure 4.5 on page 34 match the Welch's ANOVA wedge concentration spread, with the 0°, 240°, and 300° wedges having the most activity across both. There is a difference in that the 0°-60° wedge in the model has a slightly higher concentration than the 240°-300° wedge (27.5% and 28%, respectively) while the relationship is reversed in the ANOVA concentrations found for CN, as shown in Appendix A.

Table 4.3

Comet Garradd Model Parameters

Parameter Name	Value	Source
Radius	5.6 km	Boissier et al. 2013 [6]
Outflow velocity	1-25 m/s	Mazzotta et al. 2016 [29]
Solar Vector Angle	139°	NASA Horizons
Rotation period	8 hours	Custom parameter
Active Area Fraction	49.5%	Random parameter
Primary Rotation Axis	$\pi/6$	Random Parameter
Number of test cases	75	Result

Table 4.4

Observation times for 2009/P1 Garradd

Observation Label	Start Time (UTC)
August 21 2011	
944	02:45
946	03:12
948	03:46
950	04:16
952	04:47
958	06:18
960	06:50
962	07:21
964	07:53
966	08:26
968	08:59
August 22 2011	
1028	02:53
1029	03:08
1034	04:34
1035	04:46
1039	05:52
1042	06:35
1046	07:40
1051	09:01
1054	09:39

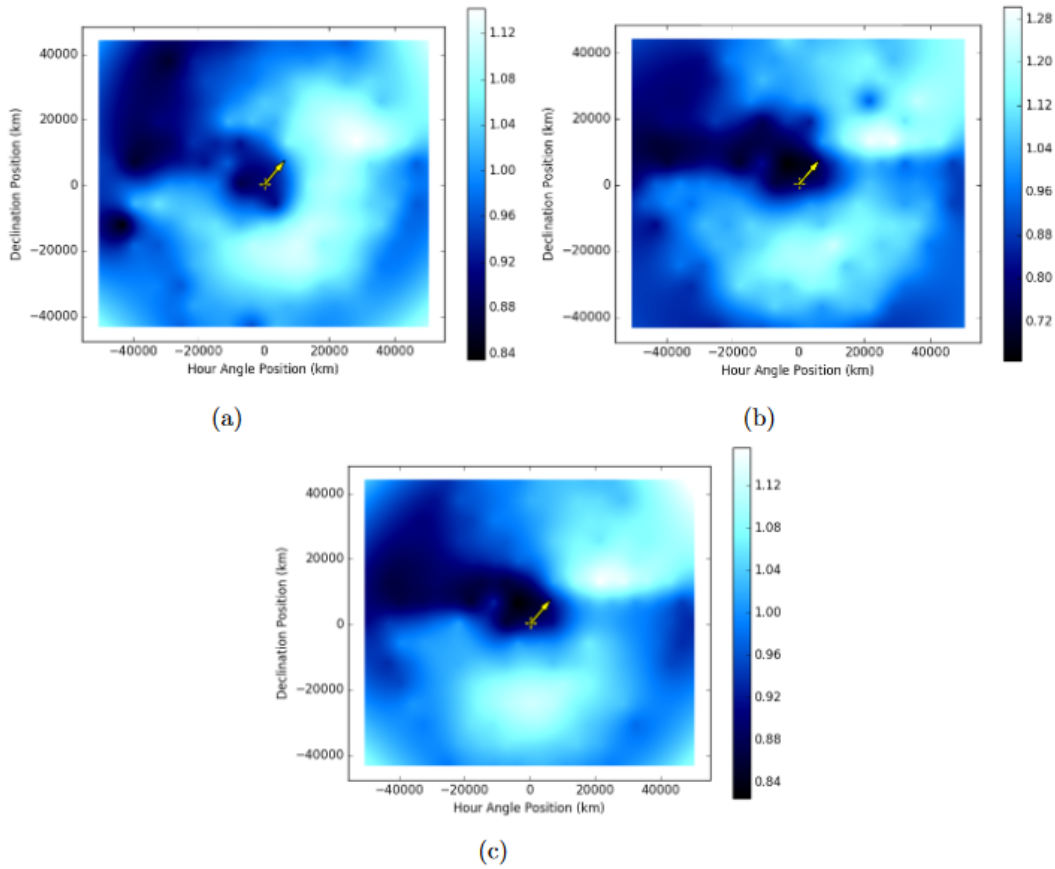

Figure 4.4

Radial division maps for Comet Garradd

Observations taken on the night of 2011 August 21 at 06:18 local time. The color bars represent the column density of the detected radical. The white feature that can be seen in the upper right is present for most of the night's observations. This suggests an active region rich in carbon-based molecules. The small yellow crosses represent the locations of the optocenter, and the arrows represent the direction of the solar vector. The solar vectors are pointing mostly out of the screen. The maps depict C_2, C_3, and CN, respectively.

While the spatial distributions of the carbon-bearing radicals are very similar to each other, NH_2 exhibits a very different outgassing behavior for Garradd. Two coma features can be seen opposite to each other on the top and bottom parts of the enhancement plots, similar in appearance to an hourglass. This indicates that the features originate from two separate sources, with the bottom source being different than the active region responsible for the carbon-bearing radicals. These plots and their respective model simulation comparisons are shown in Figure 4.6 on page 35. The active particle spread most matches the ANOVA concentrations of the August 22 observations, with the wedges in the 60°-120° and 240°-360° regions showing the highest density (14.4%, 24.2%, and 25.7%, respectively).

Both the NH_2 and CN simulations had the same generating parameters, showing how they could have separate morphology and possible source regions and yet arise from the same rotational state. The model simulated a timespan of 292 hours with timesteps of 300 seconds. Our best comparison plots were produced from an initial parameter for rotation period of 8 ± 0.5 hours. This is lower than values obtained from other authors. Farnham et al. [12] determined a value of 10.4 ± 0.05 hours from lightcurve measurements, while Ivanova et al. [18] determined a period of 11.1 ± 0.8 hours using a cross-correlation method of tracking a morphological feature over time, similar to our own. Due to the wider number of available usable observations for Comet Garradd, an additional method for checking the period was done by determining our own lightcurve from the enhanced plots. The phase determined from this method also corresponded with a period of 8 ± 0.75 hours, which agrees with our model result. This suggests that this value is at least consistent with our own observations. The lightcurve is shown in Figure 4.7 on page 36. The discrepancy of our results from the others determined may be due to our different observation methodology.

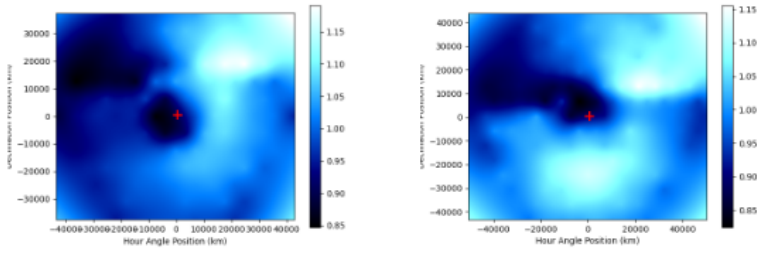

(a) 02:45:20

(b) 06:18:43

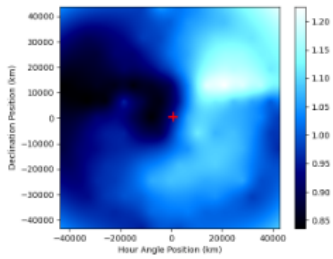

(c) 08:26:07

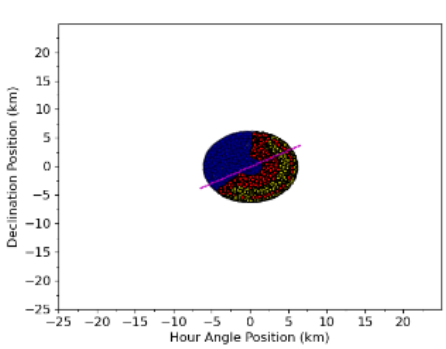

(d)

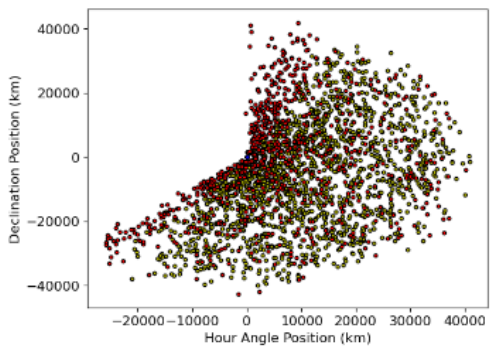

(e)

Figure 4.5

Garradd model CN comparison

Comparisons between radial division maps for *CN* in Comet Garradd and simulated maps from the Monte Carlo model. The top three images show results over the night of 2011 August 21 and their respective observation timestamps. The bottom row shows maps randomly generated by the model that appear visually closest to the enhancement plots, with the left being the initial generated nucleus and the right being the result after several timesteps. The purple line running through the nucleus in the left plot denotes the simulated primary rotation axis.

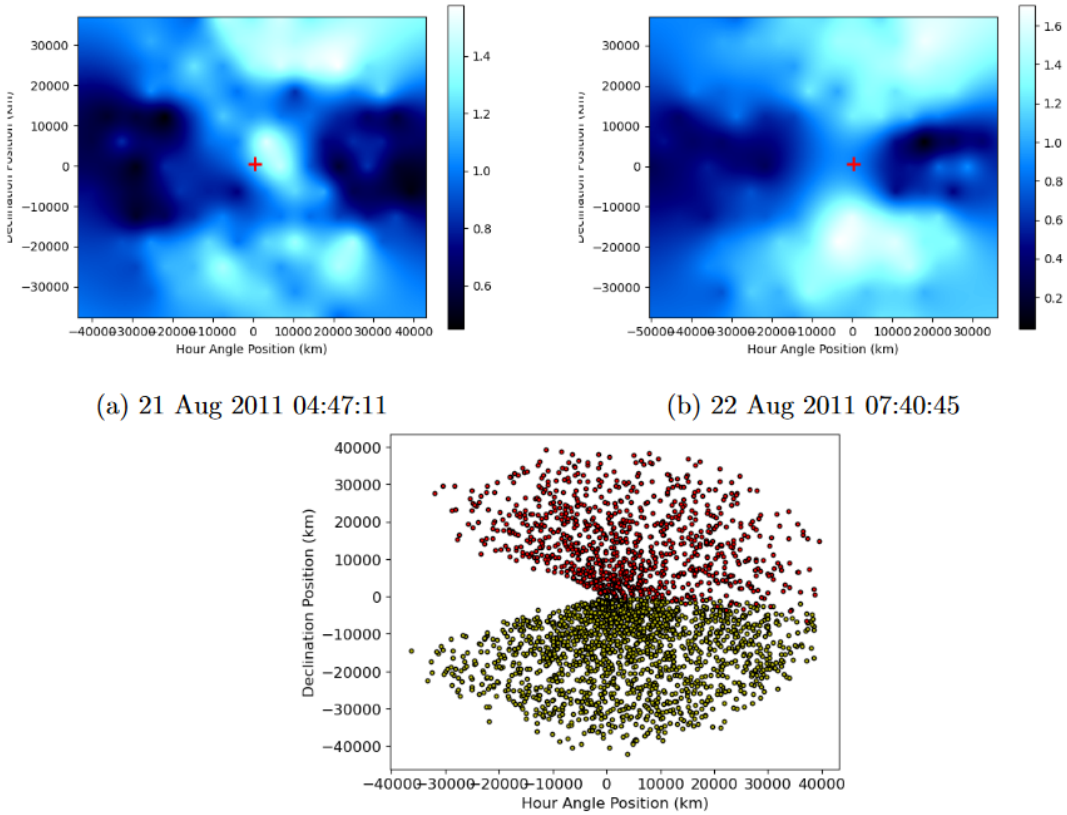

(a) 21 Aug 2011 04:47:11

(b) 22 Aug 2011 07:40:45

(c)

Figure 4.6

Garradd model NH_2 comparison

Comparisons between radial division maps for NH_2 in Comet Garradd and simulated maps from the Monte Carlo model. The top images show a sample observation over two different nights. The bottom row shows a map randomly generated by the model that appear visually closest to the enhancement plots.

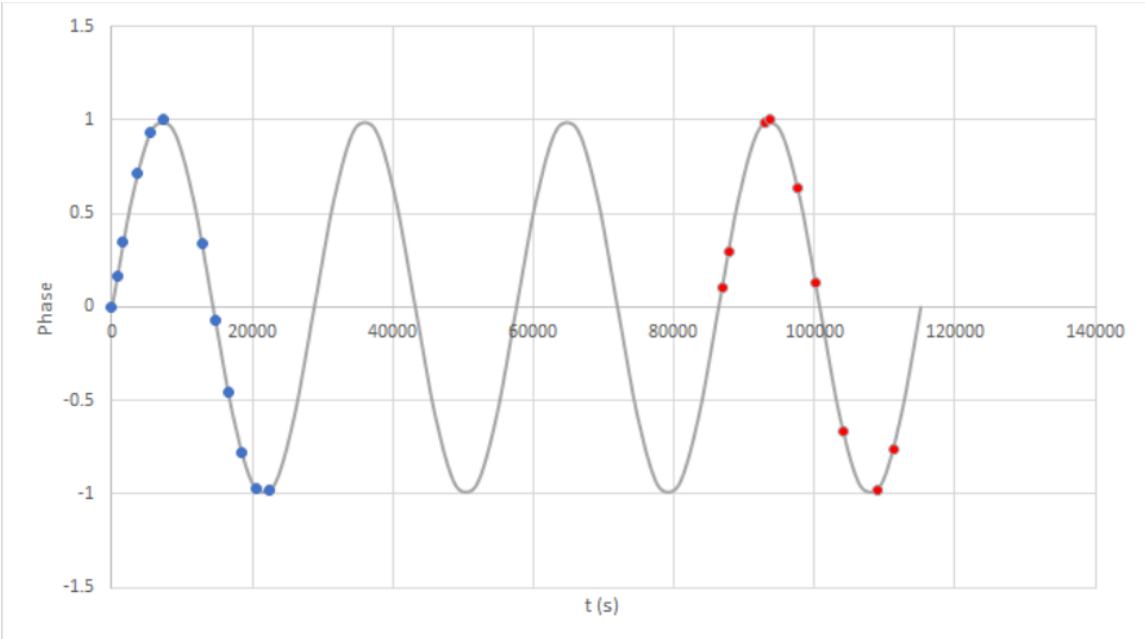

Figure 4.7

Garradd enhancement plot lightcurve

Lightcurve determined from our enhancement plots for our observations taken over two nights. The blue dot represent observations taken on August 21, red dots represent August 22. A phase (gray sine curve) was determined from similar morphological features found in the enhancements of all radicals across both nights.

4.3 168P/Hergenrother

Comet Hergenrother presented unique challenges compared to our other comets. It is another Jupiter Family Comet, whereas Garradd is a long-period comet, and thus likely has different physical properties in terms of nucleus size and active area fraction, and a lot less is known about Hergenrother as opposed to the other comets in this study. In terms of radicals, Hergenrother was found to be extremely chemically depleted [33], allowing only viable observations for CN. Only one bright feature can be seen in the CN maps, shown in Figure 4.8 on page 41, so only one active area was set in the model. Fifty runs were required for Hergenrother as well. The closest visual simulations are achieved by setting a rotation period parameter of 6.5 hours, and are shown in Figure 4.9 on page 42. The other model parameters are shown in Table 4.5 on the following page.

Table 4.5

Comet Hergenrother Model Parameters

Parameter Name	Value	Source
Radius	0.7 km	Custom parameter
Outflow velocity	1-15 m/s	Custom parameter
Solar Vector Angle	159°	NASA Horizons
Rotation period	6.5 ± 0.5 hours	Custom parameter
Active Area Fraction	19.4 ± .01%	Random parameter
Number of test cases	50	Result

Table 4.6

Observation times for 168P/Hergenrother

Observation Label	Start Time (UTC)
October 06 2012	
1200	05:09
1201	05:35
1202	06:00
1203	06:55
1204	07:18
October 08	
1307	02:57
1308	03:20
1309	03:42
1310	04:06
1314	05:39
1315	06:02
1320	08:01
October 09	
1372	02:20
1373	02:44
1377	04:18
1378	04:42
1381	05:53
1384	07:01
1389	08:55
December 19 2012	
1423	01:14
1424	01:48
December 20	
1514	06:43
December 21	
1577	01:15
1578	01:47

The active area fraction for the surface of the nucleus was 19.4 ± 0.01% for this best-match simulation. This is much lower than the best-match runs for Garradd, which coincides with our observation that Hergenrother is chemically depleted and less active compared to most comets [33]. It remains to be seen if the depletion of Hergenrother, or its recent lack of detection near its last expected perihelion [41], are related to the aforementioned fragmentation event. The model constrains the rotation period for our analysis of 168P to 6.5±0.5 hours. There are no measurements of Hergenrother's rotation period from outside sources with which to compare our result.

Due to the aforementioned chemical depletion, Welch's ANOVA wedge comparisons were done with our measurements of CN. The simulation output yield concentrations in the 0°-60°, 60°-120°, and 300°-360° wedges of 36.1%, 32%, and 28.5%, respectively. The actual ANOVA calculations show higher wedge concentrations primarily in the 0°-60°, 240°-300°, and 300°-360° regions, differing slightly from our model. This indicates that our model results may not align to our observations with high precision. It is difficult to further constrain, as almost half of our Hergenrother observations were dominated by a low signal-to-noise ratio, which can affect the amount of usable fibers in the ANOVA calculations.

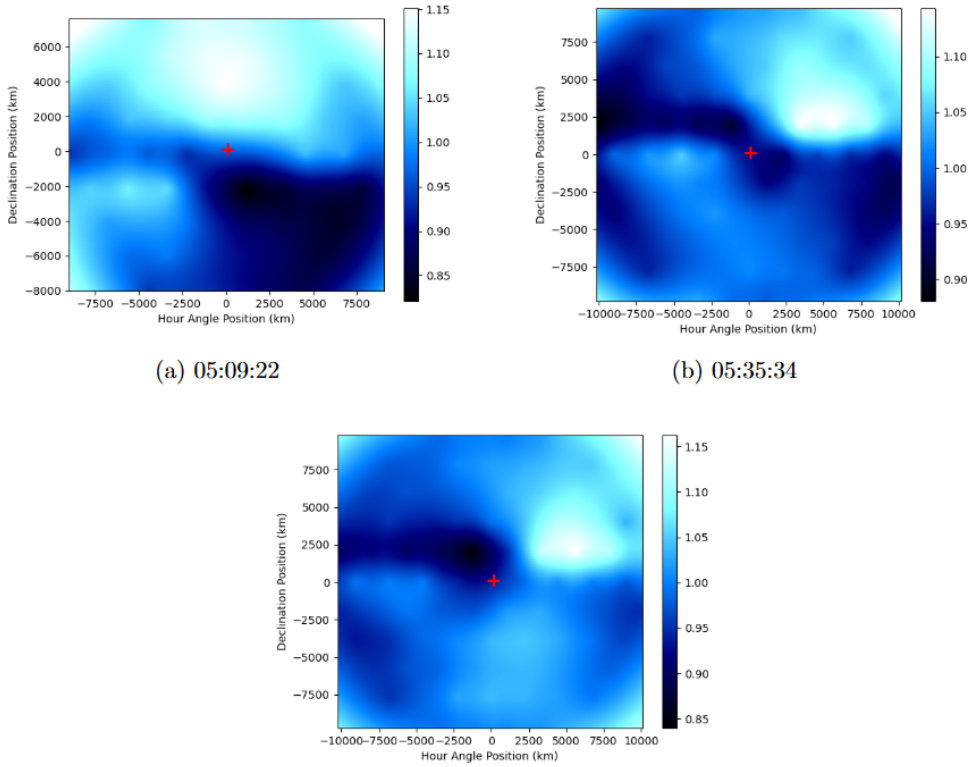

(a) 05:09:22

(b) 05:35:34

(c) 06:55:20

Figure 4.8

Hergenrother maps

CN radial division maps for Comet Hergenrother on the night of 2012 October 6. Due to the small interval of time coverage of the observations shown, the singular bright feature in the upper right of each map moves very little between images.

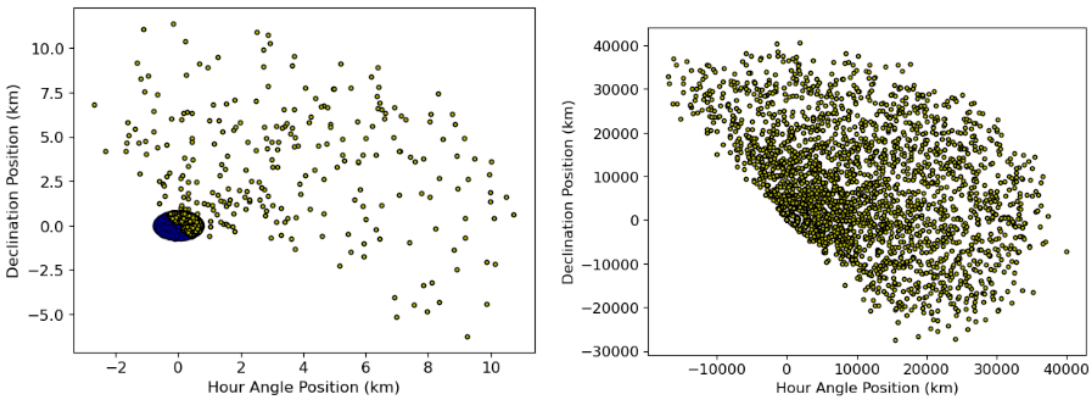

Figure 4.9

Hergenrother model CN comparison

Plots for Comet Hergenrother from the Monte Carlo model. The first image shows one of the earliest time-steps for the simulation, while the last shows the resultant plot after a simulated passage of about 290 hours. The purple line running through the nucleus in the left plot denotes the simulated primary rotation axis.

CHAPTER V

CONCLUSION AND FUTURE WORK

The rotational period parameters that were set for the best-matching model results for each comet were very close to the period constrained by either other sources or by visually tracking the periods over multiple observations. The model also simulates possible active area fractions for the comets and their approximate locations on the surface. These parameters are not well constrained by observation alone, so these values can be of interest to other parties. The values determined for active area fractions (34%, 50%, and 19% for Tempel 2, Garradd, and Hergenrother respectively) suggests that long period comets like Garradd have higher active area fractions than JFC's such as Tempel 2 and Hergenrother, as they have experienced more outgassing and perihelion passages.

Other methods of visually inferring rotational states of comets involves working with data taken via multiple observations over a long timespan, typically months apart. The data for our comets were only collected over a couple concurrent nights by the George and Cynthia Mitchell IFU Spectrograph, limiting the long-term comparisons that could be done with our model. As such our model results are only effective as comparisons with specific "snapshots" of the comets' behavior. Further constraints could be placed with further observations, especially comparing pre- and post-perihelion activity.

Future efforts will be spent on improving the model. Dust and gas are two very different components of comet composition and exhibit different outflow behavior, especially beyond the first few kilometers after release from the nucleus. Our reduced division maps from the IFU spectrograph are based primarily on the gas located in the outer coma, and we must be cautious in establishing a link to the dust outflow from the nucleus generated by the Monte Carlo model. While both may come from similar jet sources, gas interactions typically require parent-daughter molecule interactions. A possible method of improvement would be to implement techniques from a similar Monte Carlo model by Lederer et al. [25], in which trajectories of parent molecules are tracked, and possible daughter decays are simulated by a exponential decay function. The daughter molecules are ejected isotropically from the parent, and both are subsequently tracked vectorially in the coma [25]. Additionally, the current version of the Monte Carlo model only accounts for simple rotation around a primary axis. A more realistic model can be attempted by accounting for more complex rotational states, such as precession and nutation, that have been observed for other comets, such as Hartley 2 [4]. The comet's translational motion as it moves along its orbital path around the Sun could also be considered to eliminate residual outflow between timesteps. Further checks must also be made to ensure uniqueness of our model simulations, as multiple three-dimensional configurations of active area locations could theoretically produce visually similar two-dimensional plots. The parameters of the model can be adjusted accordingly as more information on our comets is corroborated and published by outside sources.

REFERENCES

[1] M. F. A'Hearn, R. L. Millis, D. G. Schleicher, D. J. Osip, and P. V. Birch, "A taxonomic survey of comet composition 1985-2004 using CCD spectroscopy," *Icarus*, vol. 118, no. 2, 1995, pp. 223–270.

[2] W. J. Altenhoff et al., "Radio continuum observations of Comet C/1999 S4 (LINEAR) before, during, and after break-up of its nucleus," *Astronomy and Astrophysics*, vol. 391, no. 1, 2002, pp. 353–360.

[3] K. Altwegg, H. Balsiger, and S. A. Fuselier, "Cometary Chemistry and the Origin of Icy Solar System Bodies: The View After Rosetta," *Annual Review of Astronomy and Astrophysics*, vol. 57, 2019, pp. 113–155.

[4] M. J. S. Belton et al., "The complex spin state of 103P/Hartley 2: Kinematics and orientation in space," *Icarus*, vol. 222, no. 2, 2013, pp. 595–609.

[5] D. Bodewits et al., "The Evolving Activity of the Dynamically Young Comet C/2009 P1 (Garradd)," *The Astrophysical Journal*, vol. 786, no. 1, 2014.

[6] J. Boissier, D. Bockelée-Morvan, O. Groussin, et al., "Millimetre continuum observations of comet C/2009 P1 (Garradd)," *Astronomy and Astrophysics*, vol. 557, 2013, pp. 1045–1056.

[7] A. L. Cochran, E. S. Barker, and C. L. Gray, "Thirty years of cometary spectroscopy from McDonald Observatory," *Icarus*, vol. 218, no. 1, 2012, pp. 144–168.

[8] M. A. Cordiner et al., "Unusually High CO Abundance of the First Active Interstellar Comet," *Nature Astronomy*, vol. 4, no. 4, 2020, pp. 861–866.

[9] J. E. Elsila, D. P. Glavin, and J. P. Dworkin, "Cometary glycine detected in samples returned by Stardust," *Meteoritics and Planetary Science*, vol. 44, no. 9, 2009, pp. 1323–1330.

[10] V. V. Emel'yanko, D. J. Asher, and M. E. Bailey, "The fundamental role of the Oort cloud in determining the flux of comets through the planetary system," *Monthly Notices of the Royal Astronomical Society*, vol. 381, no. 2, 2007, pp. 779–789.

[11] P. A. Esterle, *The Rotation State of Comet P/Halley: The End of the Debate?*, master's thesis, University of Maryland, 1994.

[12] T. Farnham, D. Bodewits, M. F. A'Hearn, and L. M. Feaga, "Deep Impact MRI Observations Of Comet Garradd (C/2009 P1)," *DPS Meeting #44*. American Astronomical Society, 2012, id. 506.05.

[13] L. M. Feaga et al., "Uncorrelated Volatile Behavior During the 2011 Apparition of Comet C/2009 P1 Garradd," *The Astronomical Journal*, vol. 147, no. 1, 2014.

[14] M. C. Festou, P. Drossart, J. Lecacheux, T. Encrenaz, F. Puel, and J. L. Kohl-Moreira, "The light curve of P/Halley and the rotation of its nucleus," *Proceedings of the International Symposium on the Diversity and Similarity of Comets*. ESA, 1987, pp. 695–701.

[15] U. Fink, "A taxonomic survey of comet composition 1985-2004 using CCD spectroscopy," *Icarus*, vol. 201, no. 1, 2009, pp. 311–334.

[16] E. Hadamcik and A. C. Levasseur-Regourd, "Imaging polarimetry of comet 73P/Schwassmann-Wachmann 3 main fragments during its 2006 apparition," *Planetary and Space Science*, vol. 123, 2016, pp. 51–62.

[17] G. J. Hill et al., "Design, construction, and performance of VIRUS-P: the prototype of a highly replicated integral-field spectrograph for HET," *Proceedings, Ground-based and Airborne Instrumentation for Astronomy II*, vol. 7014, 2008.

[18] O. Ivanova, V. Rosenbush, V. Afanasiev, and N. Kiselev, "Polarimetry, photometry, and spectroscopy of comet C/2009 P1 (Garradd)," *Icarus*, vol. 284, 2017, pp. 167–182.

[19] G. Jones, M. M. Knight, et al., "The Science of Sungrazers, Sunskirters, and Other Near-Sun Comets," *Space Science Reviews*, vol. 214, no. 20, 2017.

[20] H. Keller et al., "Comet P/Halley's nucleus and its activity," *Astronomy and Astrophysics*, vol. 187, no. 1-2, 1987, pp. 807–823.

[21] M. M. Knight, T. L. Farnham, D. G. Schleicher, and E. W. Schwieterman, "The Increasing Rotation Period of Comet 10P/Tempel 2," *The Astronomical Journal*, vol. 141, no. 1, 2011.

[22] M. M. Knight and D. G. Schleicher, "CN Morphology Studies of Comet 103P/Hartley 2," *The Astronomical Journal*, vol. 141, no. 6, 2011.

[23] M. M. Knight, D. G. Schleicher, T. L. Farnham, E. W. Schwieterman, and S. R. Christensen, "A Quarter-century of Observations of Comet 10P/Tempel 2 at Lowell Observatory: Continued Spin-down, Coma Morphology, Production Rates, and Numerical Modeling," *The Astronomical Journal*, vol. 144, no. 5, 2012.

[24] P. L. Lamy, I. Toth, H. A. Weaver, M. F. A'Hearn, and L. Jorda, "Properties of the nuclei and comae of 13 ecliptic comets from Hubble Space Telescope snapshot observations," *Astronomy and Astrophysics*, vol. 508, no. 2, 2009, pp. 1045–1056.

[25] S. M. Lederer, H. Campins, and D. J. Osip, "Chemical and physical properties of gas jets in comets. I. Monte Carlo model of an inner cometary coma," *Icarus*, vol. 199, no. 2, 2009, pp. 477–483.

[26] H. F. Levison, A. Morbidelli, C. V. Laerhoven, R. Gomes, and K. Tsiganis, "Origin of the Structure of the Kuiper Belt during a Dynamical Instability in the Orbits of Uranus and Neptune," *Icarus*, vol. 196, no. 1, 2008, pp. 258–273.

[27] D. C. Lis, D. Bockelée-Morvan, R. Güsten, et al., "Terrestrial deuterium-to-hydrogen ratio in water in hyperactive comets," *Astronomy and Astrophysics*, vol. 625, no. L5, 2009.

[28] C. M. Lisse, M. F. A'Hearn, M. G. Hauser, et al., "Infrared Observations of Comets by COBE," *The Astrophysical Journal*, vol. 496, no. 2, 1998, pp. 971–991.

[29] E. E. Mazzotta et al., "Photometry of the Oort Cloud comet C/2009 P1 (Garradd): Pre-perihelion observations at 5.7 and 2.5 AU," *Planetary and Space Science*, vol. 132, 2016, pp. 23–31.

[30] A. J. McKay, A. L. Cochran, M. A. DiSanti, et al., "Evolution of H_2O, CO, and CO_2 production in Comet C/2009 P1 Garradd during the 2011–2012 apparition," *Icarus*, vol. 250, 2015, pp. 504–515.

[31] B. E. A. Mueller, N. H. Samarasinha, and M. J. S. Belton, "The Diagnosis of Complex Rotation in the Lightcurve of 4179 Toutatis and Potential Applications to Other Asteroids and Bare Cometary Nuclei," *Icarus*, vol. 158, no. 2, 2002, pp. 305–311.

[32] J. Oort, "The Structure of the Cloud of Comets Surrounding the Solar System, and a Hypothesis Concerning its Origin," *Bulletin of the Astronomical Institutes of the Netherlands*, vol. 11, 1950, pp. 91–110.

[33] D. M. Pierce and A. L. Cochran, "Examination of Fragment Species in the Comae of Several Comets Using an Integral Field Unit Spectrograph," *The Planetary Science Journal*, vol. 2, no. 1, 2021, p. 19.

[34] G. Rinaldi et al., "Cometary coma dust size distribution from in situ IR spectra," *Monthly Notices of the Royal Astronomical Society*, vol. 469, no. 2, 2017, pp. S598–S605.

[35] D. G. Schleicher and L. M. Woodney, "Analyses of dust coma morphology of Comet Hyakutake (1996 B2) near perigee: outburst behavior, jet motion, source region locations, and nucleus pole orientation," *Icarus*, vol. 162, no. 1, 2003, pp. 190–213.

[36] Z. Sekanina and P. W. Chodas, "Fragmentation Hierarchy of Bright Sungrazing Comets and the Birth and Orbital Evolution of the Kreutz System. I. Two-Superfragment Model," *The Astrophysical Journal*, vol. 607, no. 1, 2004.

[37] A. Shannon, A. P. Jackson, and M. C. Wyatt, "Oort cloud asteroids: collisional evolution, the Nice Model, and the Grand Tack," *Monthly Notices of the Royal Astronomical Society*, vol. 485, no. 4, 2019, pp. 5511–5518.

[38] K. Tsiganis, R. Gomes, A. Morbidelli, and H. F. Levison, "Origin of the orbital architecture of the giant planets of the Solar System," *Nature*, vol. 435, 2005, pp. 459–461.

[39] C. M. Vaughan, *Jet morphology and coma analysis of comet 103P/Hartley 2*, doctoral dissertation, Mississippi State University, 2015.

[40] F. L. Whipple, "A Comet Model. I. The acceleration of Comet Encke," *The Astrophysical Journal*, vol. 111, 1950, pp. 375–394.

[41] Q. Ye, M. S. P. Kelley, and D. Bodewits, "Overdue Return of Comet 168P/Hergenrother," *The Astronomer's Telegram*. 2019, 12955.

APPENDIX A

MEAN CONCENTRATIONS OF RADICAL SPECIES

A.1 Tempel 2

The means of the concentration value Ω used in Welch's ANOVA test are shown in the following tables. Each table corresponds to a wedge in the region of the outer coma. Each wedge measures 60° in the hour angle/declination plane. Each table shows values for four of the five radical species (C_2, C_3, CN, and NH_2) measured by the spectrograph, organized by observation time. The observations for CH had too low of a signal-to-noise ratio to be used. The columns are divided by Ω_{avg} representing the mean Ω value for that wedge region, and σ representing the standard deviation for the concentration for that radical.

Table 1: Concentration Group Averages for Wedge at 0°

Date	File	C_2		C_3		CN		NH_2	
2010	No.	Ω_{avg}	σ	Ω_{avg}	σ	Ω_{avg}	σ	Ω_{avg}	σ
15 July	278	0.731	0.064	0.572	0.074	0.717	0.067	0.764	0.347
15 July	279	0.739	0.083	0.704	0.174	0.764	0.119	0.678	0.165
15 July	280	0.772	0.106	0.702	0.172	0.778	0.129	0.693	0.164
15 July	285	0.759	0.074	0.595	0.088	0.723	0.076	0.642	0.091
13 Sep	400	0.752	0.070	0.604	0.159	0.654	0.090	0.677	0.259
13 Sep	401	0.753	0.077	0.631	0.101	0.656	0.081	0.737	0.217
13 Sep	402	0.766	0.079	0.689	0.140	0.676	0.098	0.765	0.214
13 Sep	407	0.754	0.078	0.666	0.121	0.660	0.075	0.760	0.199
13 Sep	408	0.763	0.073	0.670	0.125	0.670	0.078	0.780	0.309

Table 2: Concentration Group Averages for Wedge at 60°

Date	File	C_2		C_3		CN		NH_2	
2010	No.	Ω_{avg}	σ	Ω_{avg}	σ	Ω_{avg}	σ	Ω_{avg}	σ
15 July	278	0.769	0.076	0.653	0.115	0.739	0.061	0.719	0.131
15 July	279	0.739	0.083	0.618	0.098	0.704	0.057	0.712	0.143
15 July	280	0.738	0.063	0.645	0.131	0.712	0.055	0.716	0.123
15 July	285	0.779	0.079	0.643	0.124	0.722	0.072	0.696	0.107
13 Sep	400	0.774	0.080	0.722	0.172	0.692	0.108	0.953	0.285
13 Sep	401	0.739	0.067	0.575	0.106	0.632	0.064	0.807	0.240
13 Sep	402	0.778	0.081	0.739	0.127	0.695	0.100	0.927	0.261
13 Sep	407	0.757	0.067	0.647	0.010	0.670	0.070	0.982	0.220
13 Sep	408	0.742	0.071	0.730	0.137	0.672	0.063	0.917	0.399

Table 3: Concentration Group Averages for Wedge at 120°

Date	File	C_2		C_3		CN		NH_2	
2010	No.	Ω_{avg}	σ	Ω_{avg}	σ	Ω_{avg}	σ	Ω_{avg}	σ
15 July	278	1.047	0.090	1.180	0.176	1.009	0.089	1.106	0.187
15 July	279	0.928	0.095	0.867	0.125	0.870	0.086	0.879	0.104
15 July	280	0.933	0.090	0.876	0.135	0.879	0.081	0.897	0.010
15 July	285	1.017	0.121	1.187	0.319	0.990	0.161	0.967	0.203
13 Sep	400	1.020	0.089	1.075	0.155	0.999	0.124	1.145	0.213
13 Sep	401	0.935	0.107	0.880	0.154	0.891	0.131	1.044	0.268
13 Sep	402	1.010	0.088	1.058	0.128	1.001	0.119	1.145	0.155
13 Sep	407	0.985	0.098	0.960	0.132	0.964	0.119	1.167	0.200
13 Sep	408	0.983	0.088	1.004	0.130	0.971	0.112	1.195	0.241

Table 4: Concentration Group Averages for Wedge at 180°

Date	File	C_2		C_3		CN		NH_2	
2010	No.	Ω_{avg}	σ	Ω_{avg}	σ	Ω_{avg}	σ	Ω_{avg}	σ
15 July	278	1.300	0.089	1.495	0.173	1.304	0.094	1.338	0.147
15 July	279	1.252	0.107	1.334	0.185	1.227	0.140	1.265	0.214
15 July	280	1.240	0.107	1.315	0.184	1.221	0.132	1.253	0.231
15 July	285	1.258	0.071	1.452	0.097	1.283	0.070	1.294	0.119
13 Sep	400	0.774	0.080	0.722	0.172	0.692	0.108	0.953	0.285
13 Sep	401	0.739	0.067	0.575	0.106	0.632	0.064	0.807	0.240
13 Sep	402	0.778	0.081	0.739	0.127	0.695	0.100	0.927	0.261
13 Sep	407	0.757	0.067	0.647	0.010	0.670	0.070	0.982	0.220
13 Sep	408	0.742	0.071	0.730	0.137	0.672	0.063	0.917	0.399

Table 5: Concentration Group Averages for Wedge at 240°

Date	File	C_2		C_3		CN		NH_2	
2010	No.	Ω_{avg}	σ	Ω_{avg}	σ	Ω_{avg}	σ	Ω_{avg}	σ
15 July	278	1.185	0.121	1.205	0.231	1.233	0.126	1.172	0.229
15 July	279	1.291	0.083	1.396	0.130	1.348	0.096	1.482	0.220
15 July	280	1.265	0.095	1.365	0.136	1.326	0.083	1.423	0.239
15 July	285	1.249	0.050	1.327	0.072	1.303	0.040	1.422	0.120
13 Sep	400	1.235	0.098	1.311	0.213	1.354	0.147	1.192	0.319
13 Sep	401	1.310	0.094	1.512	0.181	1.480	0.139	1.263	0.175
13 Sep	402	1.219	0.089	1.242	9.285	1.332	0.145	1.206	0.285
13 Sep	407	1.245	0.083	1.350	0.148	1.360	0.130	1.205	0.213
13 Sep	408	1.237	0.091	1.269	0.145	1.350	0.129	1.193	0.230

Table 6: Concentration Group Averages for Wedge at 300°

Date	File	C_2		C_3		CN		NH_2	
2010	No.	Ω_{avg}	σ	Ω_{avg}	σ	Ω_{avg}	σ	Ω_{avg}	σ
15 July	278	0.902	0.068	0.781	0.091	0.940	0.087	0.860	0.184
15 July	279	1.031	0.102	1.071	0.159	1.100	0.123	1.021	0.197
15 July	280	1.015	0.102	1.046	0.152	1.074	0.120	1.020	0.205
15 July	285	1.017	0.078	0.970	0.137	1.053	0.095	1.081	0.157
13 Sep	400	0.947	0.097	0.835	0.202	0.917	0.129	0.760	0.261
13 Sep	401	0.999	0.115	1.019	0.217	0.993	0.188	0.851	0.272
13 Sep	402	0.958	0.084	0.885	0.170	0.928	0.127	0.790	0.278
13 Sep	407	0.966	0.097	0.961	0.164	0.943	0.132	0.797	0.286
13 Sep	408	0.975	0.084	0.948	0.175	0.938	0.126	0.670	0.400